Naval Research Laboratory

Washington, DC 20375-5320

NRL/MR/5307--19-9839

3D MIMO Radar Prototype for UAV Swarming, Tracking, and Collision Avoidance: Karle Fellowship Final Report

Brian B. Tierney

Advanced Concepts Group
Radar Division

March 11, 2019

DISTRIBUTION STATEMENT A: Approved for public release; distribution is unlimited.

REPORT DOCUMENTATION PAGE

Form Approved
OMB No. 0704-0188

Public reporting burden for this collection of information is estimated to average 1 hour per response, including the time for reviewing instructions, searching existing data sources, gathering and maintaining the data needed, and completing and reviewing this collection of information. Send comments regarding this burden estimate or any other aspect of this collection of information, including suggestions for reducing this burden to Department of Defense, Washington Headquarters Services, Directorate for Information Operations and Reports (0704-0188), 1215 Jefferson Davis Highway, Suite 1204, Arlington, VA 22202-4302. Respondents should be aware that notwithstanding any other provision of law, no person shall be subject to any penalty for failing to comply with a collection of information if it does not display a currently valid OMB control number. **PLEASE DO NOT RETURN YOUR FORM TO THE ABOVE ADDRESS.**

1. REPORT DATE *(DD-MM-YYYY)*
11-03-2019

2. REPORT TYPE
Memorandum Report

3. DATES COVERED *(From - To)*
Aug 2016 - Aug 2018

4. TITLE AND SUBTITLE

3D MIMO Radar Prototype for UAV Swarming, Tracking, and Collision Avoidance: Karle Fellowship Final Report

5a. CONTRACT NUMBER

5b. GRANT NUMBER

5c. PROGRAM ELEMENT NUMBER
NISE

6. AUTHOR(S)

Brian B. Tierney

5d. PROJECT NUMBER

5e. TASK NUMBER

5f. WORK UNIT NUMBER
N2K1

7. PERFORMING ORGANIZATION NAME(S) AND ADDRESS(ES)

Naval Research Laboratory
4555 Overlook Avenue, SW
Washington, DC 20375-5344

8. PERFORMING ORGANIZATION REPORT NUMBER

NRL/MR/5307--19-9839

9. SPONSORING / MONITORING AGENCY NAME(S) AND ADDRESS(ES)

Naval Research Laboratory
4555 Overlook Avenue, SW
Washington, DC 20375-5344

10. SPONSOR / MONITOR'S ACRONYM(S)

NRL - NISE

11. SPONSOR / MONITOR'S REPORT NUMBER(S)

12. DISTRIBUTION / AVAILABILITY STATEMENT

DISTRIBUTION STATEMENT A: Approved for public release; distribution is unlimited.

13. SUPPLEMENTARY NOTES

14. ABSTRACT

This report details the work performed by Dr. Brian B. Tierney during his Karle Fellowship. His research focused on the design of a low-cost, multi-input multi-output (MIMO) radar prototype capable of 3D sensing (range, azimuth and elevation) for UAV applications such as swarming, track-and-pursuit, and collision avoidance.

15. SUBJECT TERMS

Millimeter-Wave Radar
Antenna Arrays
Unmanned Aerial Vehicles (UAVs)

16. SECURITY CLASSIFICATION OF:			**17. LIMITATION OF ABSTRACT**	**18. NUMBER OF PAGES**	**19a. NAME OF RESPONSIBLE PERSON**
					Brian B. Tierney
a. REPORT	**b. ABSTRACT**	**c. THIS PAGE**	Unclassified Unlimited	32	**19b. TELEPHONE NUMBER** *(include area code)*
Unclassified Unlimited	Unclassified Unlimited	Unclassified Unlimited			(202) 767-3459

Standard Form 298 (Rev. 8-98)
Prescribed by ANSI Std. Z39.18

This page intentionally left blank.

1. PREFACE

This report details the work performed by Dr. Brian B. Tierney during the two years of his Karle Fellowship. His research focused on the design of a low-cost, multi-input multi-output (MIMO), FMCW radar prototype capable of 3D sensing (range, azimuth, and elevation) for UAV applications such as swarming, track-and-pursuit, and collision avoidance.

2. BACKGROUND

The DoD has recently established aggressive goals for the development of unmanned and autonomous systems. Autonomous applications include target pursuit, formation flight, terminal guidance, and collision avoidance. However, sensor solutions that enable these applications have thus far focused on: (i) cameras, which are ineffective in darkness, sun glare, rain, and fog; (ii) GPS, which can be denied or spoofed; and (iii) surface radar, which is either too expensive or too inaccurate.

Millimeter-wave (mmW) radar performs well in degraded visual environments. It can also be small enough and cheap enough to mount onto a UAV for onboard sensing. For his Karle Fellowship, Dr. Brian Tierney has adapted automotive mmW radar technology to meet the requirements of autonomous UAV systems. Several design challenges have arisen from such adaptation, such as utilizing a limited number of antenna channels to scan in both azimuth and elevation.

This final report documents Dr. Brian Tierney's research over the course of the two years of his Karle Fellowship. The first half of the report discusses the design of Prototype 1, which was designed in the first year of the Karle Fellowship. The second half of the report discusses the design of Prototype 2, which was designed in the second year of the Karle Fellowship.

3. PROTOTYPE 1 - DESIGN REQUIREMENTS

UAV swarming algorithms require the ability to perceive relative range and bearing of UAV peers within the swarm. Typically, the members of the swarm are displaced in azimuth, rather than elevation. Therefore, these swarming algorithms require a broad field of view and good angular estimation in azimuth while tolerating a narrower field of view and lower fidelity angular estimation in elevation. With this in mind, the design requirements for Prototype 1 are as follows:

- Broad field-of-view in azimuth
- High-fidelity angular estimation in azimuth
- Adequate ($\approx 20°$) field-of-view in elevation
- Maintain high antenna gain

By sacrificing performance in elevation, antenna gain can be improved without the need to include additional antennas. This reduces the cost of the sensor with minimal sacrifice to performance for the aforementioned UAV applications.

Manuscript approved January 29, 2019.

4. PROTOTYPE 1 - HARDWARE DESIGN

To expedite the development of our mmW radar prototype, the radar hardware was purchased from Inras GmbH, an Austrian company founded by a professor instrumental in the development of SiGe-based automotive radar technology. Inras develops modular, frequency-modulated continuous-wave (FMCW), multi-input multi-output (MIMO) radar prototypes for frequencies ranging from 5.8 to 77 GHz [1]. The idea is that the modular design allows for the rapid testing of particular components of a radar system, such as mmW ICs, signal processing blocks, or antennas. The modular system is shown in Fig. 1.

Inras also sells complete evaluation platforms at frequencies of 24 and 77 GHz based on prior-generation ICs available from Infineon. We purchased the 77 GHz system and designed our own custom MIMO antenna array for our UAS application. The antenna design is discussed in Section 5.

Fig. 1 - Inras modular radar test bed.

The Inras radar is an FMCW MIMO system employing digital beamforming. The hardware block diagram of the system is provided in Fig. 2. A linearly-modulated chirp waveform is generated and transmitted sequentially by the four transmit (TX) antennas, as shown in Fig. 3, to enable MIMO processing techniques. The signals reflected by nearby targets are received by the 16 receive (RX) channels and down-converted to baseband frequencies using stretch processing, i.e. the received signal is mixed directly with the chirp waveform. The output frequencies of the mixer can be directly related to the target range using the following well-known equation:

$$Range = \frac{c\tau f_B}{2\beta} \tag{1}$$

Here, c is the speed of light, τ is the duration of the linear modulation, β is the bandwidth of the linear modulation, and f_B is the output frequency of the mixer. Each of the 16 RX channels is then sampled digitally using its own RX chain, which consists of low-pass filters, a variable-gain amplifier, and an analog-to-digital converter (ADC). The signals can then be beamformed digitally, providing processing gain as well as the capacity for angular estimation of the target location. This will be discussed further in Sec. 7.

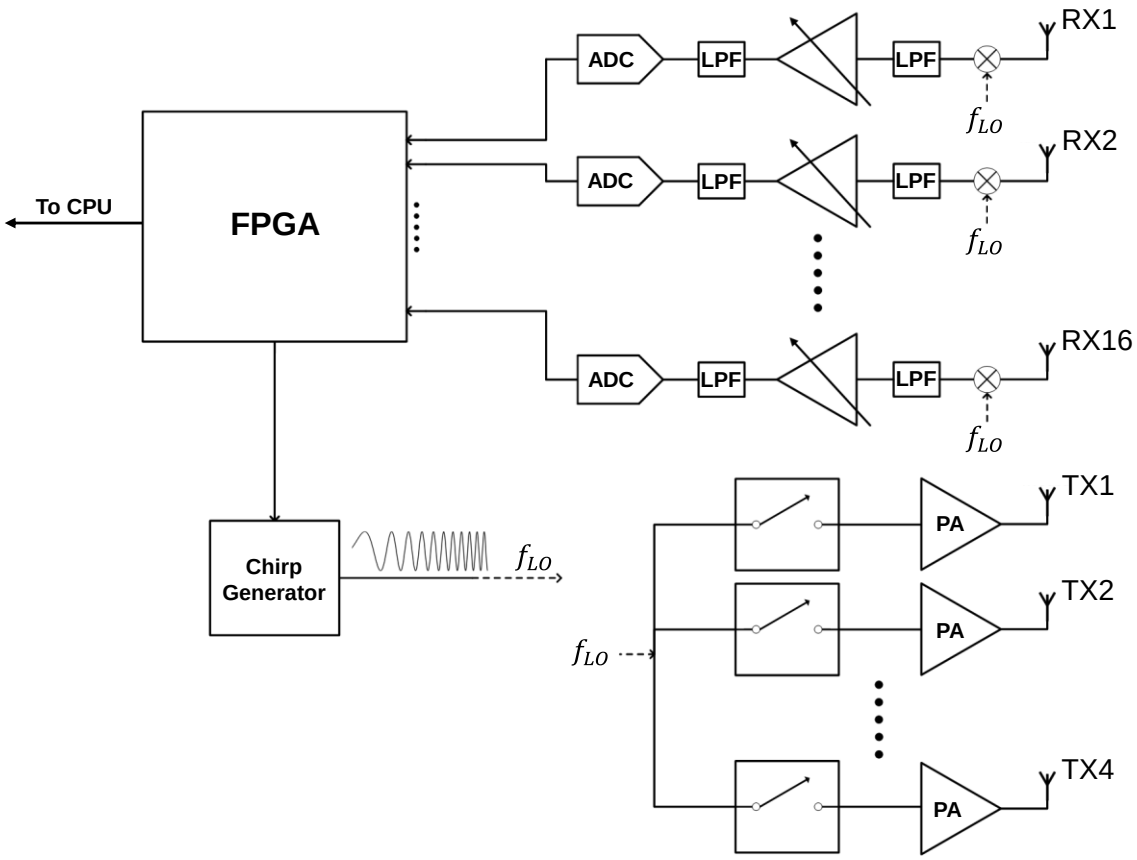

Fig. 2 - Hardware block diagram for Prototype 1. A linear frequency-modulated chirp signal is generated and sequentially transmitted by the array of transmit antennas. A signal reflected by a target is collected by the array of receive antennas, converted to the digital domain, and ultimately sent to a CPU.

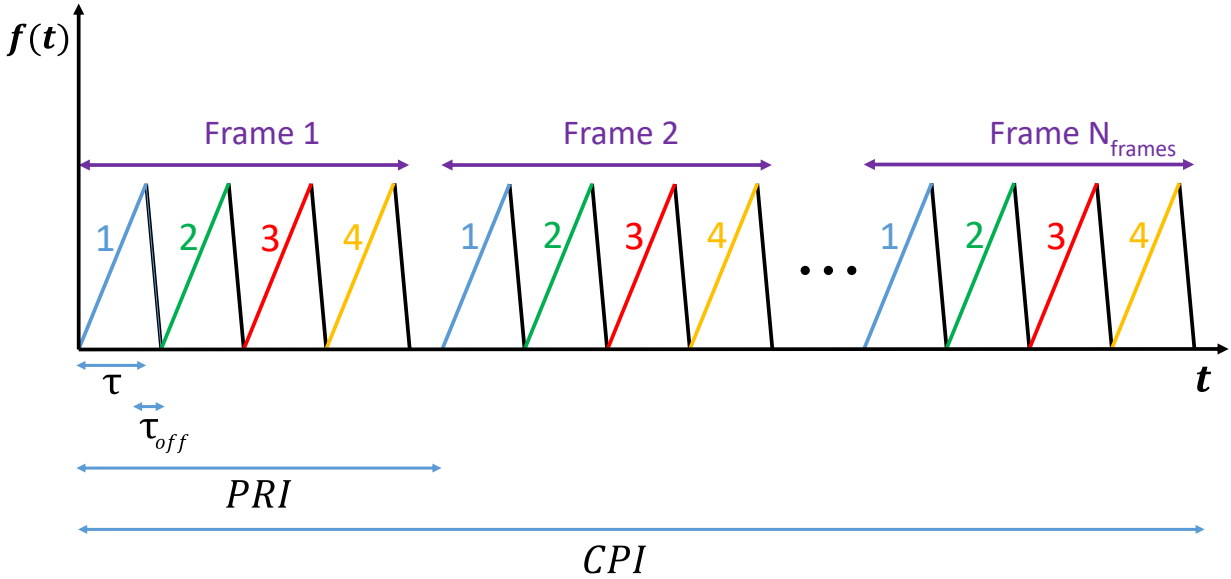

Fig. 3 - FMCW transmission waveforms for Prototype 1. A linear frequency-modulated chirp is sequentially transmitted by the array of 4 transmit antennas. This time-division multiplexing allows MIMO processing.

The hardware used in the radar system are provided as follows:

- RF Power Amplifiers: Infineon RPN7720
- RF Receiver Chips: Infineon RRN7745
- Waveform Generation: Infineon RTN7735 and Infineon RCC1010
- ADC: Texas Instruments AFE5801
- Clock Source: Texas Instruments LMK4033
- FPGA: Arria V 5AGXMB1G4F35I5N

The waveform generation is produced using Infineon's RTN7735 transmitter chip in conjunction with its RCC1010 chip, which is a companion CMOS chip which provides a fully digital interface to the RTN7735 [2]. The waveform is amplified by Infineon's dual power amplifier RPN7720 and fed to the TX antennas. The transmit antennas can be activated sequentially by means of digital control signals. The signal received by RX antennas are fed to Infineon's RRN7745 receiver chips, which performs the stretch processing [2]. The AFE5801 ADC chips include a low-pass filter and variable-gain amplifier.

5. PROTOTYPE 1 - MIMO ANTENNA ARRAY DESIGN

The Prototype 1 hardware uses MIMO technology with a Rogers 3003 127 μm substrate [3]. Considering the design requirements of Sec. 3, the MIMO antenna array was designed as depicted in Fig. 4. Microstrip series-patch antennas were used as array elements. The 16 RX antennas are spaced vertically by $\lambda/2$ (2 mm), providing angular estimation in azimuth. The 4 TX antennas are also spaced vertically by $\lambda/2$ and horizontally by $\lambda/2$, which provides angular estimation in elevation. However, the estimation in azimuth is better than that in elevation. The scanning capabilities of the MIMO array are perhaps better understood by considering the equivalent virtual array depicted in Fig. 5, which looks similar to a standard 16 by 4 array. The dimensional asymmetry results in superior scanning in azimuth.

The radiation patterns in azimuth and elevation for a single antenna element are depicted in Fig. 6. The radiation patterns in azimuth and elevation for the entire MIMO array (using Hanning weighting) are depicted in Fig. 7. The antenna parameters of a single array element as well as the entire array were simulated using Advanced Design System (ADS) and are provided in Table 1.

As predicted by antenna array theory [4], scanning in elevation is constricted by the narrow element pattern in elevation, which is depicted in Fig. 6a. Indeed, for large beam scan angles of the array factor, the achieved angle of the main beam is actually much smaller. This aligns with the design requirements described in Sec. 3. However, this angular discrepancy does not affect angular estimation algorithms, which rely on achieving maximum received power when the array factor scan angle matches that of the target location [5]. Indeed, Fig. 8 demonstrates that this is still true.

The fabricated antenna prototype is shown in Fig. 9.

Table 1 – Antenna Parameters Simulated using Advanced Design System

	Gain (dBi)	**Radiation Efficiency**	**Elevation Beamwidth (3 dB)**	**Azimuth Beamwidth (3 dB)**
Single Element	12.9	66.9%	78°	16°
RX Array (Uniform Weighting)	23.9	74%	7°	16°
RX Array (Hanning Weighting)	22.3	74%	11°	16°
TX Array (Uniform Weighting)	19.6	72%	26°	14°

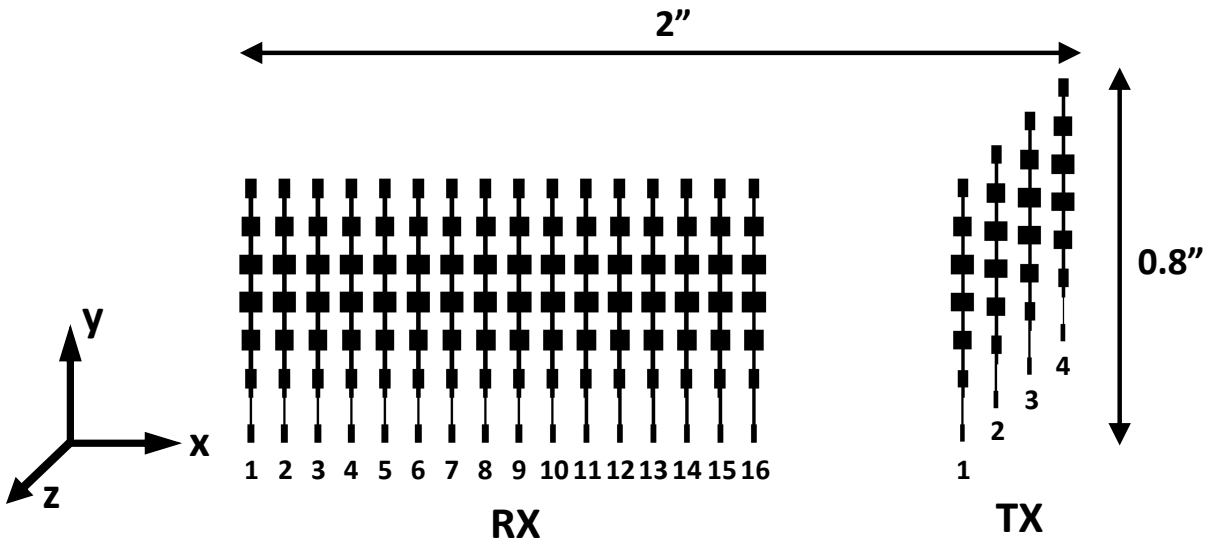

Fig. 4 – The MIMO antenna array design for Prototype 1 consisting of 16 RX antennas and 4 TX antennas. Series-fed patch antennas are used as array elements.

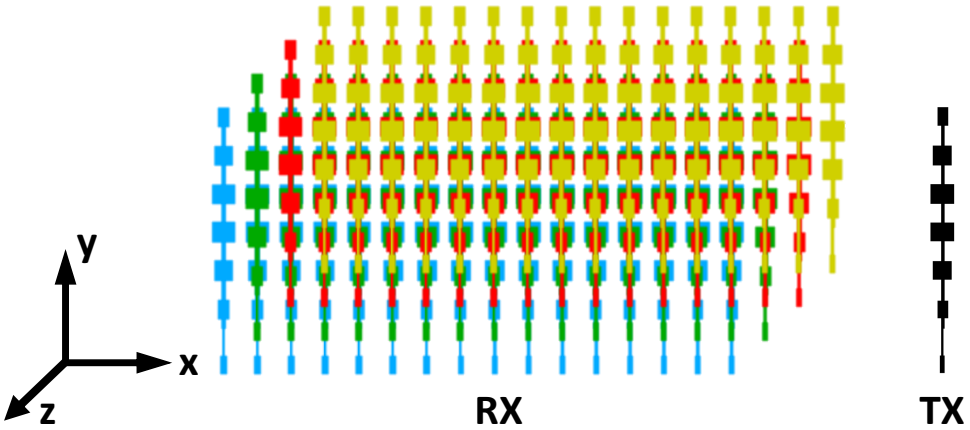

Fig. 5 - The performance of the array depicted in Fig. 4 can be equated to the virtual array depicted here. The virtual array consists of 1 TX antenna and 64 RX antennas. These RX antennas often overlap in this virtual space but are electrically isolated in physical space. The result is a compact array with beam scanning in both elevation and azimuth while maintaining high antenna gain.

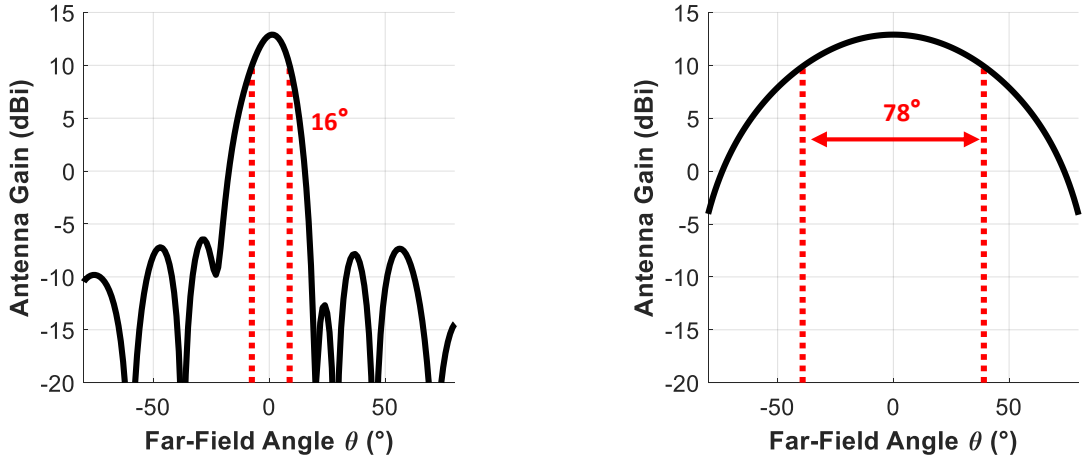

(a) Elevation Plane (ϕ = 90°) (b) Azimuth Plane (ϕ = 0°)

Fig. 6 – Simulated radiation pattern for the series-fed patch antenna array element in the (a) elevation plane and (b) azimuth plane. The simulation was performed using Advanced Design System.

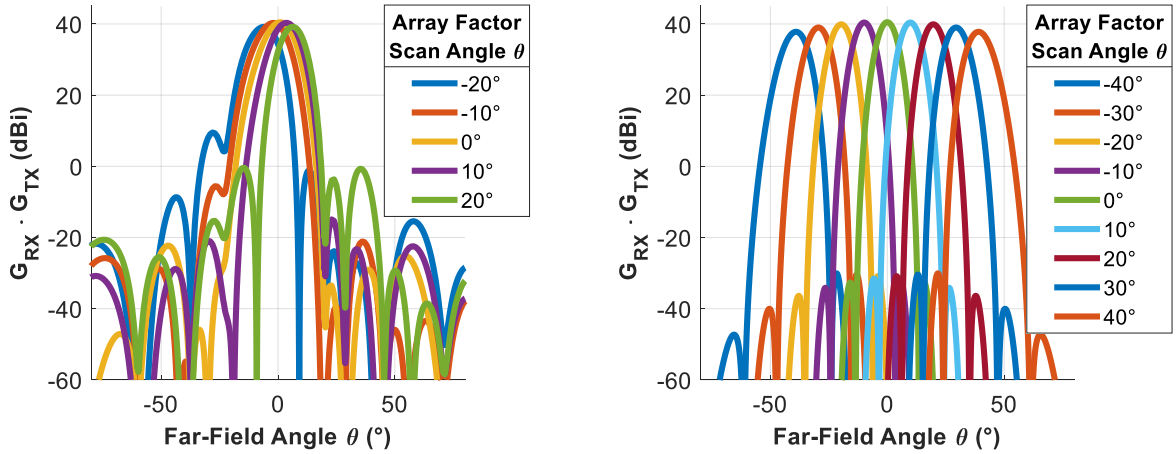

(a) Elevation Plane (ϕ = 90°) (b) Azimuth Plane (ϕ = 0°)

Fig. 7 – Two-way gain ($G_{RX} \cdot G_{TX}$) patterns calculated using antenna array theory with Hanning element weighting. The patterns are in (a) the azimuth plane and (b) the elevation plane. The narrow antenna element pattern in elevation (shown in Fig. 6a) restricts beam scanning capabilities in elevation, as indicated by the difference between the array factor scan angle and the achieved beam angle. The wide antenna element pattern in azimuth (shown in Fig. 6b) allows wide beam scanning in azimuth.

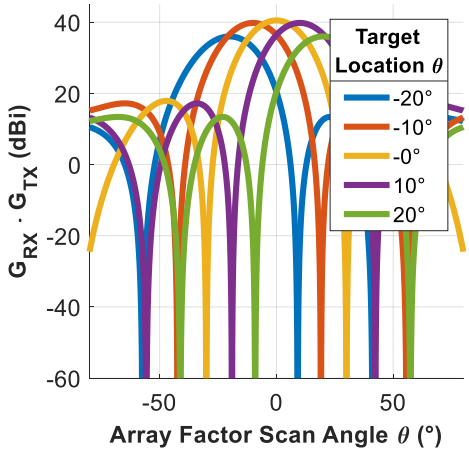

Fig. 8 - Two-way gain ($G_{RX} \cdot G_{TX}$) for a signal reflected by targets placed in the elevation plane ($\phi = 0°$) as a function of array factor scan angle θ. The peak of the gain product is achieved at the target location. Therefore, we can still use standard direction estimation algorithms.

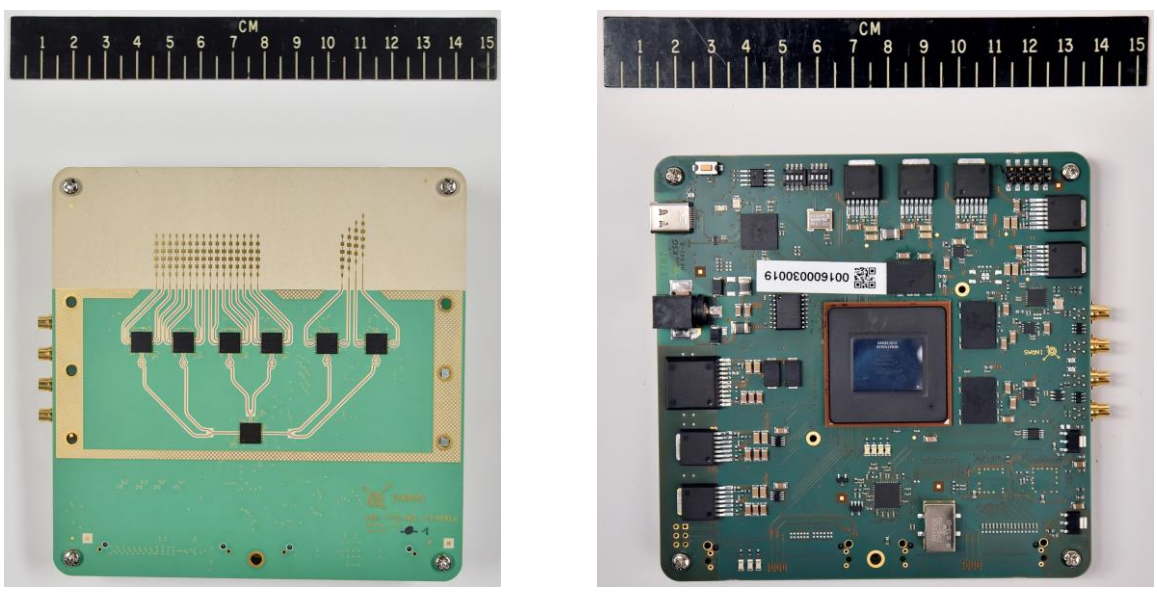

(a) Radar front end (b) Radar back end

Fig. 9 – The fabricated Inras radar prototype (Prototype 1).

6. PROTOTYPE 1 - SYSTEM ANALYSIS

The parameters of a MIMO FMCW radar system are given as follows:

- $\boldsymbol{f_0}$ − Center operating frequency of the radar.
- $\boldsymbol{P_{TX}}$ − The power transmitted from a single transmit antenna.
- $\boldsymbol{N_{TX}}$ − The number of transmit (TX) antennas used.
- $\boldsymbol{N_{RX}}$ − The number of receive (RX) antennas used.
- $\boldsymbol{G_{RX}(\theta,\phi)}$ − The RX array gain as a function of target position (θ,ϕ).
- $\boldsymbol{G_{TX}(\theta,\phi)}$ − The TX array gain as a function of target position (θ,ϕ).
- $\boldsymbol{\tau}$ − The pulse length (see Fig. 3).
- $\boldsymbol{\tau_{off}}$ − The time during which all transmitters are off (see Fig. 3).
- $\boldsymbol{\beta}$ − The bandwidth of the transmitted radar chirp.
- $\boldsymbol{PRI}$ − The time between the start of frames (pulse repetition interval). See Fig. 3.
- $\boldsymbol{N}$ − Number of digital samples per chirp.
- $\boldsymbol{N_{frames}}$ − The number of frames in a single coherent processing interval (CPI). See Fig. 3.
- $\boldsymbol{T_{scene}}$ − The noise temperature seen by the antennas.
- $\boldsymbol{F}$ − Noise figure of the receive chain.
- $\boldsymbol{L}$ − Estimated losses from the atmosphere, digital signal processing, etc.

For Prototype 1, the radar parameters are as quantified in
Table 6. The signal-to-noise ratio (SNR) of a return signal is given by the radar equation for MIMO FMCW systems [6]:

$$SNR(\theta,\phi) = \frac{P_{TX} * N_{TX} * G_{RX}(\theta,\phi) * G_{TX}(\theta,\phi) * \lambda^2 * \sigma * N_{frame} * \tau}{(4\pi)^3 * R^4 * k * T_{scene} * F * L} \tag{2}$$

Table 2 - Parameters of the Prototype 1 radar system

f_0	$76.5\ GHz$
P_{TX}	$10\ mW\ (10\ dBm)$
N_{TX}	4
N_{RX}	16
G_{RX} (at Broadside)	$22.3\ dBi$
G_{TX} (at Broadside)	$19.6\ dBi$
τ	$102.4\ \mu s$
τ_{off}	$64\ \mu s$
β	$300\ MHz$
PRI	$665.6\ \mu s$
N	512 (real samples)
N_{frames}	64
T_{scene}	$290\ K$
F	$\approx 15\ dB$
L	$\approx 2\ dB$

The additional variables in Eq. (2) are given as follows:

- $\boldsymbol{\lambda}$ – The free-space wavelength with f_0.
- $\boldsymbol{\sigma}$ – The radar cross section (RCS) of the target.
- $\boldsymbol{R}$ – The target range.
- $\boldsymbol{k}$ – Boltzmann's constant ($1.38 \cdot 10^{-23}\ m^2\ kg\ s^{-2}\ K^{-1}$).

A target detection is triggered when the SNR of a returned signal exceeds a pre-determined threshold. For the Prototype 1, we use a threshold of 10 dB coupled with binary integration (refer to Sec. 7).

Well-known equations for unambiguous range and range rate [6] are provided here:

$$Unambiguous\ Range = \frac{N * c}{4 * \beta} \tag{3}$$

$$Unambiguous\ Range\ Rate = \frac{c}{4 * PRI * f_0} \tag{4}$$

For radar parameters provided in
Table 6, the unambiguous range and range rate are 128 meters and 1.47 m/s, respectively. However, disambiguation techniques, such as the Chinese Remainder Theorem or finite-difference techniques, can be used to extend discernable range and range rate [6].

The range resolution [6] of the radar is provided here:

$$Range\ Resolution = \frac{c}{2\beta} \tag{5}$$

For the parameters provided in
Table 6, the range resolution is 0.5 meters. Note, however, that this is not the same as the accuracy of the range prediction. Indeed, the accuracy of range estimation can surpass the range resolution. Rather, this quantifies how well we can separate two targets in range. The range resolution is also equal to the size of the range bins, unless zero padding is employed. Otherwise, the equation is given by (6):

$$Range\ Bin\ Size = \frac{N * c}{2 * \beta * N_{FFT}} \tag{6}$$

Here, N_{FFT} is the length of the FFT (including zero padding) in fast time. For the system presented in this report, zero padding is not employed.

7. PROTOTYPE 1 - SIGNAL PROCESSING

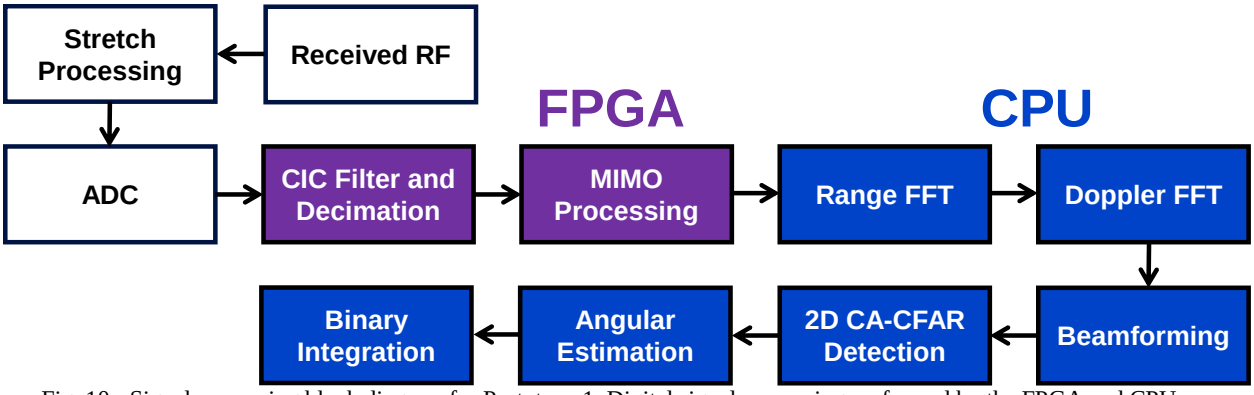

Fig. 10 - Signal processing block diagram for Prototype 1. Digital signal processing performed by the FPGA and CPU are depicted by the purple and blue boxes, respectively.

The employed signal processing block diagram is depicted in Fig. 10. As depicted in Fig. 2, the received RF signal is mixed down to baseband frequencies and subsequently sampled by the analog-to-digital converter (ADC). Prototype 1 actually samples the signal at a much higher rate than specified in

Table 6, but subsequently feeds the samples through a CIC filter and decimation stage. The intent of this oversampling is to reduce the quantization noise of the ADC [7]. A decimation rate of 8 is employed for the system described in this report, resulting in an ADC sampling frequency of 40 MHz.

After decimation, MIMO processing is performed by the FPGA. For the time-division multiplexing scheme employed (see Fig. 3), this amounts simply to separating the received signal based on what transmitter is currently active. The FPGA then transfers the data stream to a CPU to perform the more complicated signal processing routines.

The CPU first performs an FFT in both fast time (range) and slow time (Doppler) to generate a 2D range-Doppler map. Hanning windows are used for both FFTs. The MIMO virtual channels are then beamformed digitally to produce beams at a grid of angles. A Hanning window is used to weight the elements of the antenna array along its x-axis. The grid of angles are given as follows:

- **Elevation Angles:** -15° to 15° by 5° increments
- **Azimuth Angles:** -35° to 35° by 5° increments

This 2D grid consists of 105 angles. After the 105 beams are formed, a 2D CA-CFAR (cell-averaging constant false alarm rate) algorithm is employed on each beam. The algorithm simply uses a standard 1D CA-CFAR algorithm in both dimensions and then registers as a detection any range-Doppler bin that exceeds the SNR threshold in both dimensions. Two-dimensional centroiding is used to cluster detections together. The parameters of this CA-CFAR step are provided here:

- **Number of Guard Cells**: 3 in range, 3 in Doppler
- **Number of Averaging Cells**: 3 in range, 3 in Doppler
- **Centroid Window Size**: 2 in range, 2 in Doppler
- **SNR threshold**: 10 dB in range, 10 dB in Doppler

After the CA-CFAR stage, the angular estimation algorithm from [5] is employed. The algorithm uses Newton's method to perform a maximum-likelihood angle estimation with computational efficiency.

Finally, binary integration [6] is performed. Binary integration essentially keeps only detections which are present during M of N consecutive CPI. Detections from consecutive CPI are considered to be from the same target if they have similar range, angle, and Doppler. For the system described in this report, $M = 2$ and $N = 4$.

8. PROTOTYPE 1 - MEASUREMENT RESULTS

To demonstrate the 3D sensing capability of the radar system, experiments were performed at the AFRL test site in Stockbridge, NY. The sensor was mounted to the bottom of a DJI S1000, referred to hereafter as the host drone. A DJI Flame Wheel was used as the target drone. The host drone was programmed to hover at a fixed altitude of 30 meters while maintaining a fixed heading. The target drone was programmed to hover at a variety of programmed GPS waypoints, dwelling at each waypoint while the radar collected and stored data for that waypoint.

The radar was mounted such that the x-axis (see Fig. 4) was positioned vertically. This was originally done for terrain-following experiments. However, to avoid confusion, the results presented in this section will be presented in the sensor coordinate system depicted in Fig. 4.

Fig. 11 presents registered detections from the target drone while it hovered at a series of prescribed locations in the x-y plane at a range of 20 meters from the sensor. For Fig. 11a, 13 prescribed positions at 2 meter spacing along the x-axis were used. For Fig. 11b, 5 prescribed positions at 3 meter spacing along the y-axis were used, but only 4 positions were captured within the field of view. At each position, data from 24 CPIs were collected. Note that the true position of the target drone with respect to the sensor was subject to some systematic error from the GPS and compass of the DJI S1000. It is clear that estimation of the angle has larger variance along the y-axis, as expected by the design of the antenna array. Nevertheless, the sensor is clearly capable of angular estimation in both axes.

Of course, the sensor can also measure the range of the target. Fig. 12 presents registered detections from the target drone while it hovered at broadside over a series of prescribed ranges spaced every 10 meters. The target was only detectable out to 50 meters.

Table 3 provides the average standard deviation of the measurements provided in Fig. 11 and Fig. 12. The values are calculated by averaging the measurement variance and subsequently taking the square root. Note, however, that slight motion of the drone during the measurement may artificially inflate these variance estimates. Note also that the variance of the angular estimation will vary with SNR. The SNR of the detections depicted in Fig. 11 and Fig. 12 varied primarily between 15 and 20 dB.

Table 3 – Standard deviation of 3D measurements shown in Fig. 11 and Fig. 12

$\sigma_{elevation}$	0.61°
$\sigma_{azimuth}$	2.6°
σ_{range}	0.13 meters

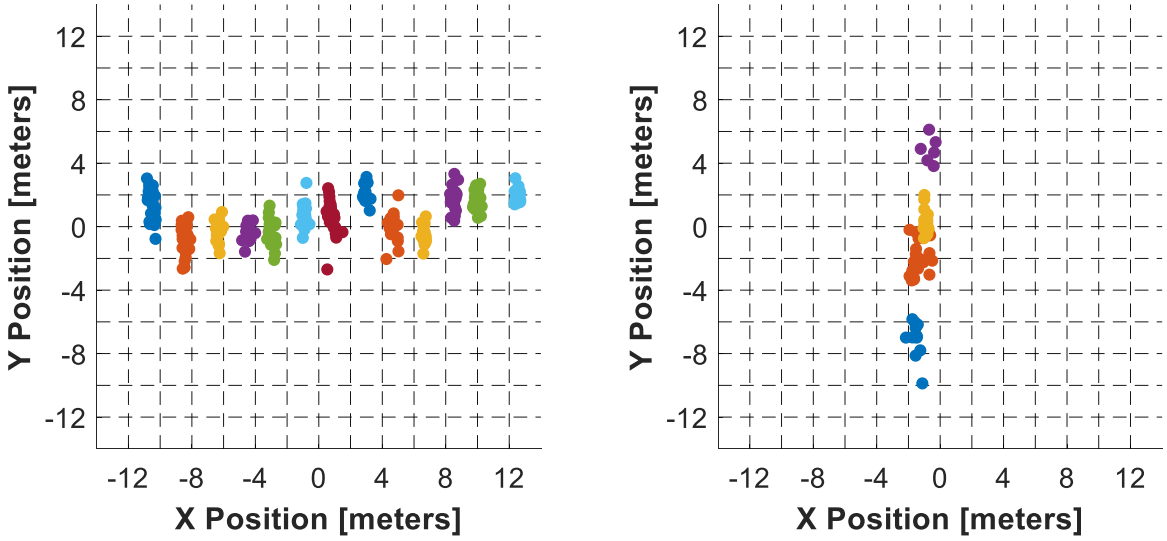

(a) (b)

Fig. 11 - Detections from a DJI Flame Wheel drone hovering at a series of prescribed locations along the (a) x axis and (b) y axis of the sensor coordinate system (see Fig. 4). The DJI Flame Wheel was positioned 20 meters in range (z-axis) from the DJI S1000. The prescribed drone locations in (a) were separated by 2 meters while the locations in (b) were separated by 3 meters. Note that the true position of the target drone was subject to some small error in the prescribed GPS waypoint and the heading of the host drone.

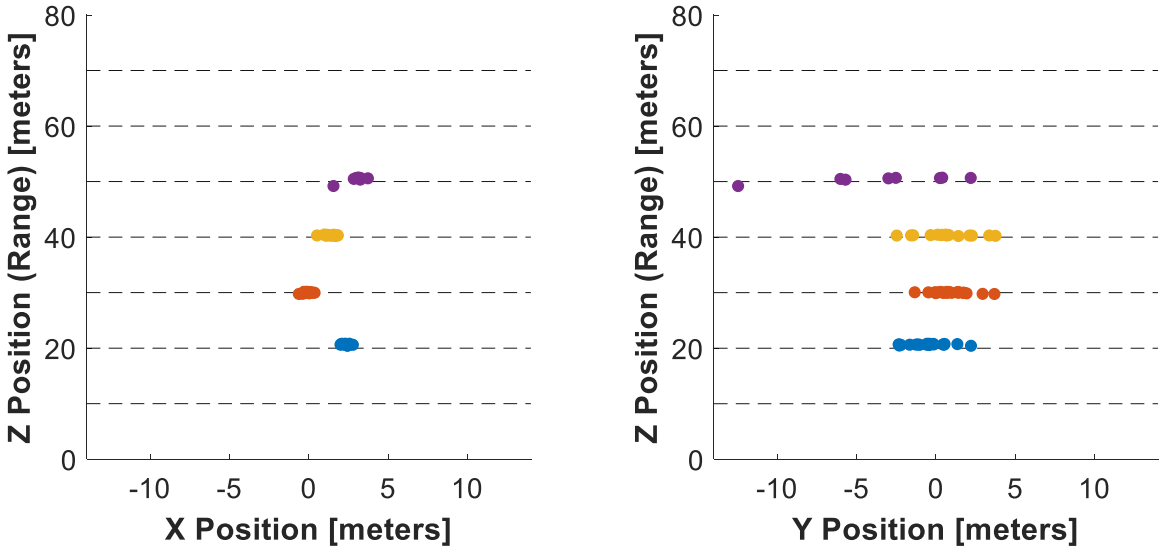

(a) (b)

Fig. 12 – Detections from a DJI Flame Wheel drone hovering at a series of prescribed locations in range. The detections are shown in both the (a) x-z plane and (b) y-z plane of the sensor coordinate system (see Fig. 4).

9. SHORTCOMINGS OF PROTOTYPE 1

Many shortcomings of Prototype 1 were discovered during the course of this work that we hope to address in future work. Some of the shortcomings are listed here:

- **Limited Signal Processing –** The FPGA firmware included by Inras is very limited. As depicted in Fig. 10, most of the signal processing had to be performed with a computer. Although programming signal processing routines on a CPU is easier, performing the routines on an FPGA would allow real-time detections. These detections could be fed to flight control algorithms to perform tasks such as real-time tracking. Unfortunately, the FPGA firmware on the Inras system could not easily be altered.
- **Limited PRI** – We discovered experimentally that the actual PRI of the Inras sensor does not agree with the PRI that was advertised. In particular, the achieved PRI of the sensor appears to be larger than we stipulate. This limitation reduces the achievable signal processing gain and therefore reduces the range of the sensor. It also compromises range rate measurements.
- **Binary Phase Modulation Not Available –** The sensor uses time-division multiplexing to separate the TX signals, rather than binary phase modulation. With binary phase modulation, all TX antennas are active at once but have a unique phase coding. Time-division multiplexing is simpler, but it reduces the total transmit power and therefore reduces the range of the sensor. Moreover, the PRI is longer, which reduces the unambiguous range rate, as seen by Equation (4).
- **Relatively Large –** At 5 inches by 5 inches, the Inras sensor is relatively large and heavy.
- **Limited Documentation –** The Inras system includes very limited documentation, making it difficult to work with.

10. YEAR 2 - EMERGING TECHNOLOGY

In the second year of his Karle Fellowship, Dr. Brian Tierney sought to address the shortcomings of Prototype 1 using emerging mmW integrated circuit technology from Texas Instruments and emerging GPU technology from NVidia.

10.1 Texas Instruments mmW Integrated Circuits

Recently, a new suite of mmW integrated circuits (ICs) has become available from Texas Instruments. An overview of these ICs are given in Table 4. The ICs are highly integrated, including waveform generator, mixing, digitization, and even a microcontroller (AWR1443 and AWR1642) and/or DSP (AWR1642).

The Texas Instruments suite of ICs address many of the drawbacks of Prototype 1, which was designed in the first year of the Karle Fellowship. However, it still does not directly address the signal processing limitations. With less than 2 MB of RAM and limited computational power, the ICs alone are adequate only for simple applications. For our radar system, which is looking for small targets in a larger, 3D space, the radar data must be streamed from the IC into a more powerful processing unit.

Table 4 – Parametrics for Texas Instruments mmW IC family

	AWR1443	AWR1243	AWR1642
Number of RX	4	4	4
Number of TX	3	3	2
ADC Sampling Rate (Max) (MSPS)	12.5	37.5	12.5
Arm CPU	ARM-Cortex R4F 200MHz	-	ARM-Cortex R4F 200MHz
DSP	-	-	C674x DSP 600 MHz
Hardware Accelerators	Radar Hardware Accelerator	-	-
RAM	576 kB	-	1536 kB

10.2 NVidia Embedded GPUs

Recently, NVidia has released embedded GPUs that are small enough to be integrated aboard a UAV platform. In the radar prototype, the NVidia Jetson TX2 is chosen to receive the radar data streaming from the mmW IC. Since many radar signal processing routines are highly parallelizable, the GPU provides an enormous speed advantage.

Table 5 - Parametrics for the radar system's GPU

	NVidia Jetson TX2
GPU	NVidia Pascal, 256 CUDA Cores
CPU	HMP Dual Denver 2/2 MB L2 + Quad ARM A57/2 MB L2
Memory	8 GB 128 bit LPDDR4; 59.7 GB/s
I/O Capacity	4 Radars, 1 Camera

11. PROTOTYPE 2 - SYSTEM BLOCK DIAGRAM

The radar system’s block diagram is provided in Fig. 13. The AWR1443 Texas Instruments IC generates a prescribed FMCW waveform and transmits the waveform in a time-division-multiplexed sequence using the 3 TX antennas, similar to what is shown in Fig. 3 but with 3 transmitters rather than 4 transmitters. After the signal is reflected from a nearby target, each RX channel receives the signal, mixes it with the transmitted waveform, and digitizes the signal with an ADC. Although the data is then passed to the on-chip microcontroller, the microcontroller simply passes the data on to the NVidia TX2 GPU for processing.

The signal processing routines on the GPU were written using C++ and NVidia CUDA, which is a parallel computing platform and application programming interface (API) that allows software developers to develop highly-parallelized scientific computing algorithms.

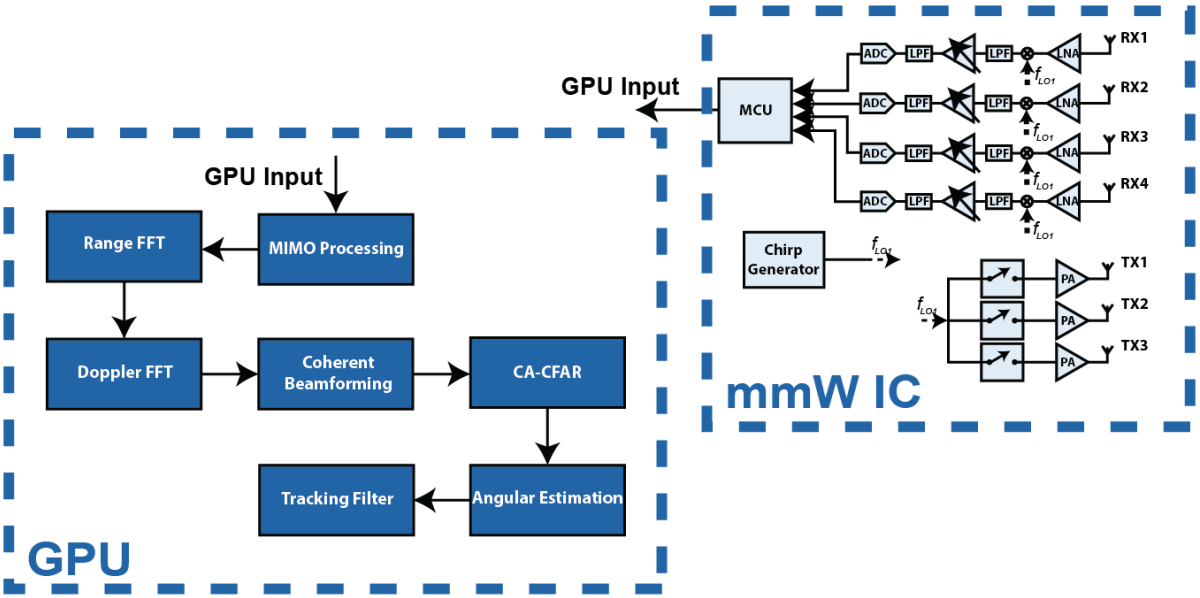

Fig. 13 - Radar system block diagram for Prototype 2

12. PROTOTYPE 2 - RADAR PARAMETERS

The parameters of a MIMO, FMCW radar system are reviewed in Section 6. The parameters of Prototype 2 (MIMO, FMCW radar system) are given as follows:

Table 6 - Parameters of Prototype 2

f_0	$78\ GHz$
P_{TX}	$15\ mW\ (12\ dBm)$
N_{TX}	3
N_{RX}	4
G_{RX} (at Broadside)	$19.6\ dBi$
G_{TX} (at Broadside)	$17.6\ dBi$
τ	$30\ \mu s$
τ_{off}	$12\ \mu s$
β	$300\ MHz$
PRI	$114\ \mu s$
N	256 (complex I/Q)
N_{frames}	128
T_{scene}	$290\ K$
F	$\approx 16\ dB$
L	$\approx 1\ dB$
Range Resolution	$0.5\ m$
Unambiguous Range	$128\ m$
Unambiguous Velocity	$8.4\ m/s$

For this radar prototype, the radar PRI is 114 μs, which is much better for detecting moving targets than the prior year's radar (PRI of 665.6 μs).

13. PROTOTYPE 2 - ANTENNA DESIGN

The Texas Instruments IC is limited to 4 RX channels and 3 TX channels. Detecting small UAVs nearby is a challenge with such a limited number of antenna channels. In this section, we present an antenna design that overcomes this challenge by using large subarray antenna elements.

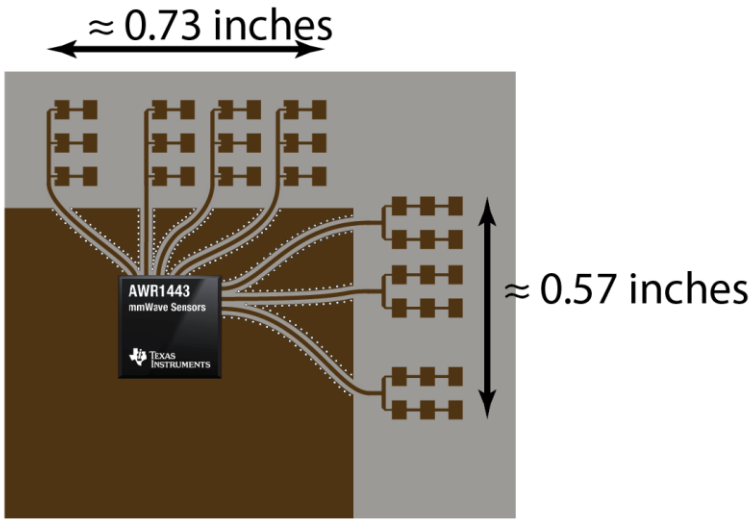

Fig. 14 - Artistic depiction of the antenna design

13.1 Array Sizing

The antenna array design is provided in Fig. 14. Each antenna subarray is comprised of a 2 by 3 grid of microstrip patches. This subarray size provides a sufficiently high gain for nearby small UAVs at the expense of a narrower field-of-view (FOV). Fig. 15 shows the two-way subarray antenna pattern in both the azimuthal plane and elevation plane. The 3-dB beamwidth is approximately 30° in both azimuth and elevation. However, for UAV tracking of a single target, this beamwidth is sufficient. Indeed, a feedback control loop can keep a gimbal-mounted radar pointed directly at the target, even if the target moves suddenly.

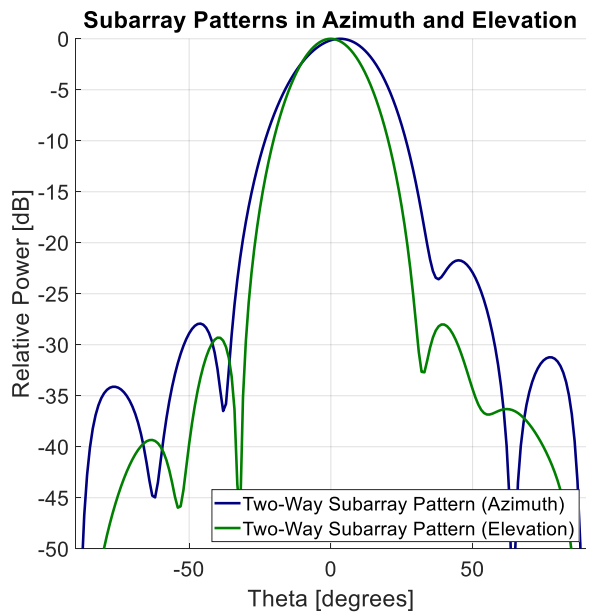

Fig. 15 – Two-way subarray antenna patterns in both the azimuthal plane and elevation plane.

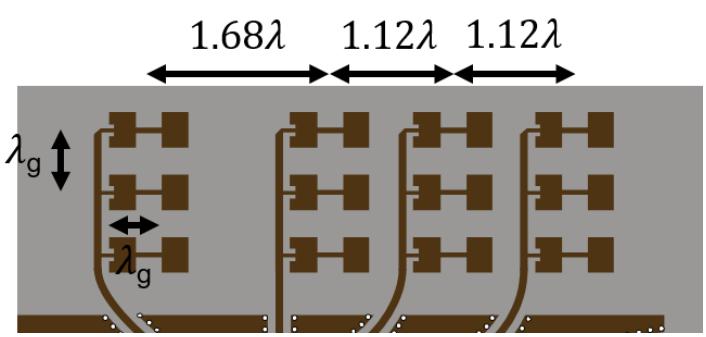

Fig. 16 - Spacing of the RX antennas. The patches of the subarray are separated by a guided wavelength (λ_g) for constructive interference at broadside.

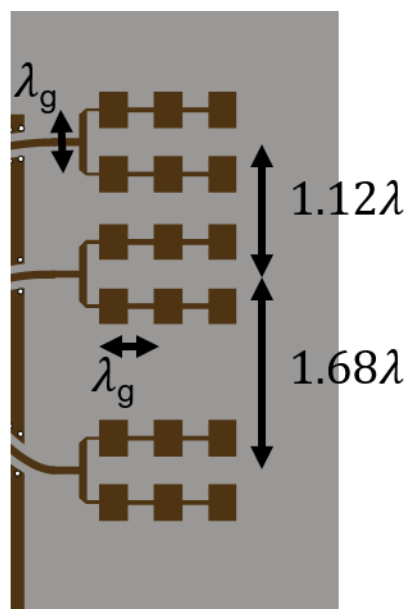

Fig. 17 - Spacing of the TX antennas. The patches of the subarray are separated by a guided wavelength (λ_g) for constructive interference at broadside.

13.2 Array Placement

Aside from the reduced FOV, the large subarray size presents another complication: the elements must be spaced by more than 0.5λ. Indeed, the minimum spacing in this design is 1.12λ, where λ is the free-space wavelength at 77 GHz. Although such a large spacing can induce a grating lobe effect in the

array factor, the grating lobes are somewhat suppressed by using a spacing of 1.68λ between two of the antennas. The array spacing is shown in Fig. 16 and Fig. 17. The resulting two-way array factor for a scan angle of 0° is provided in Fig. 18. In the azimuthal plane, where scanning is controlled by the 4 RX antennas, the grating lobe is suppressed to -2.5 dB. In the elevation plane, where scanning is controlled by the 3 TX antennas, the grating lobe is suppressed to -1.5 dB.

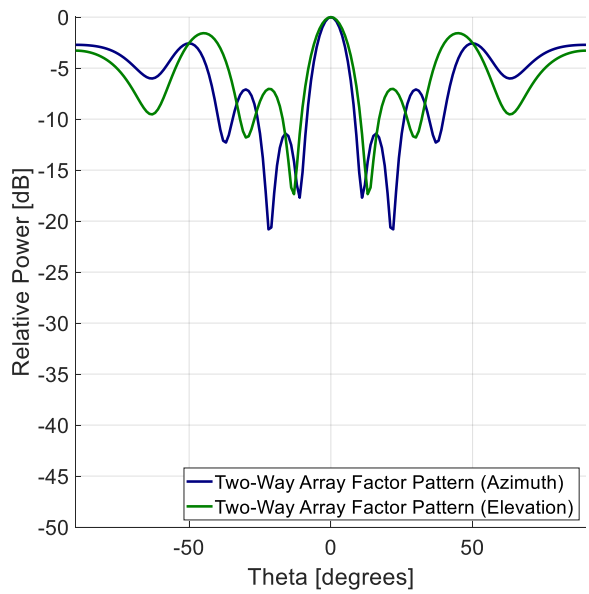

Fig. 18 – Two-way array factor patterns in both the azimuthal plane and elevation plane.

This high sidelobe level has two implications: (1) ground clutter or other sources of clutter could be illuminated by the high sidelobe and obscure the target of interest and (2) erroneous direction-of-arrival calculation. We discuss these concerns in Sections 13.2.1 and 13.2.2.

13.2.1 Obscuration by Clutter

Fig. 19 depicts the radar's overall antenna array radiation pattern, i.e. the subarray pattern multiplied by the array factor, in both the azimuthal and elevation planes. The figure shows three different array steering angles: 0°, 10°, and 20°. In each case, the phase of each antenna element is established to achieve constructive interference at the steering angle of interest. Inspection of the figure shows that for 0° and 10° steering angles, the resulting radiation pattern is a pencil-beam shape with low sidelobe levels. Thus, good angular filtering is achieved. Moreover, the high sidelobes of the array factor are filtered by the subarray pattern. However, as the radar steers to 20° and beyond, the pencil-beam quality collapses, resulting in poor angular filtering within the beamwidth of the subarray pattern. The effect is that there is greater chance that clutter illuminated by a sidelobe will obscure the target of interest.

Although this degradation of angular filtering is not desired, it is a tradeoff we are willing to make and is not detrimental to UAV application. Indeed, it there is limited clutter in our aerial UAV applications, where altitudes of operation are typically 20 to 50 meters. To reduce ground clutter further, we point the radar face away from the ground, detecting targets from a lower altitude.

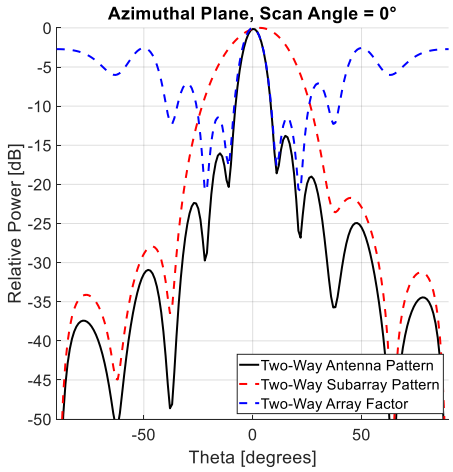

Fig. 19a

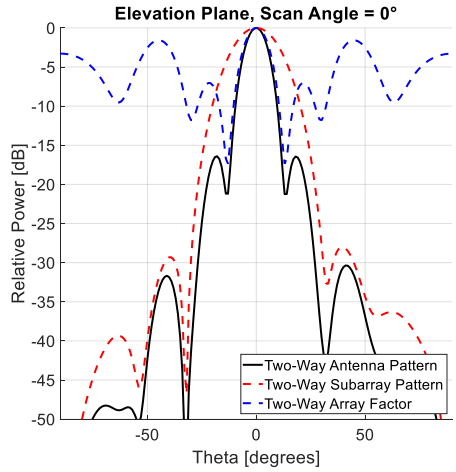

Fig. 19b

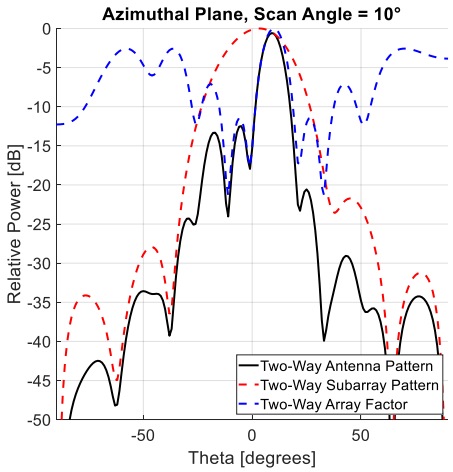

Fig. 19c

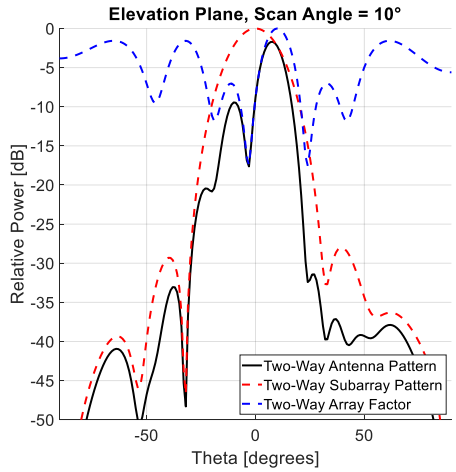

Fig. 19d

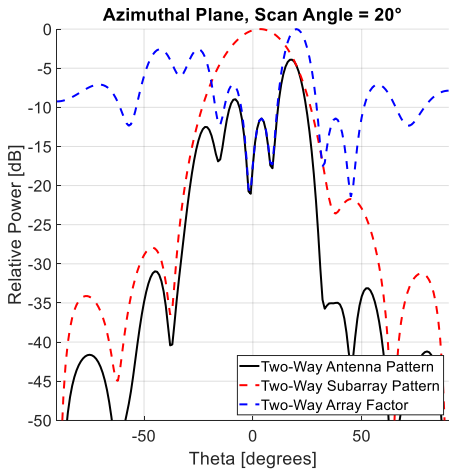

Fig. 19e

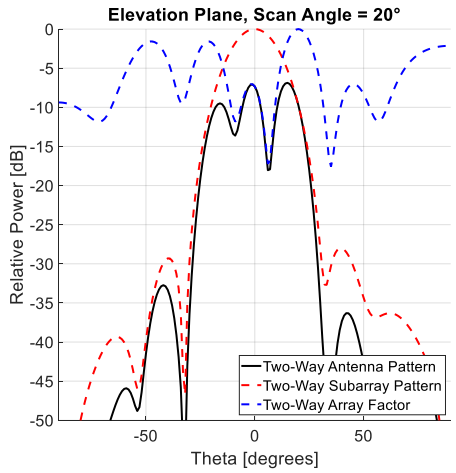

Fig. 19f

Fig. 19 – Simulated antenna patterns, subarray patterns, and array factors. As the arrays steer to 20° and farther, the antenna gain begins to drop. Although the antenna pattern becomes less of a pencil beam, this does not impact direction-of-arrival estimation, which depends only on the array factor, as discussed in Section 13.2.2.

13.2.2 Erroneous Direction-of-Arrival Calculation

The second implication of high sidelobes is erroneous direction-of-arrival estimation. The direction-of-arrival is calculated by finding the array factor scan direction that maximizes the received power from the target signal. This same technique was employed in Section 5 and can be justified using maximum likelihood analysis [5].

This technique can be implemented easily in software, due to the digital beamforming capabilities of the radar system. For example, if a target is located at 20° in azimuth and 10° in elevation, the resulting angular scan yields the plots provided in Fig. 20 (assuming no clutter or noise). Note that the relative values within the angular scan depend only on the array factor and not the subarray pattern. Although the sidelobes are somewhat large, the correct scan direction can still be determined by finding the scan direction yielding the highest received power.

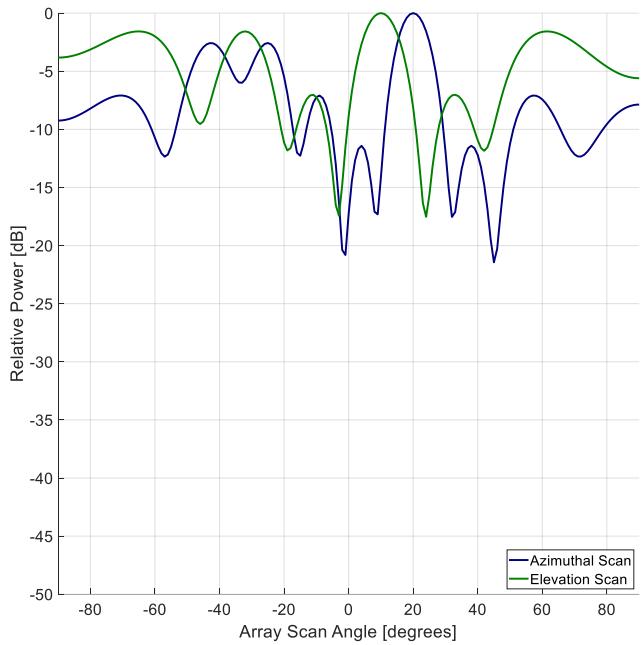

Fig. 20 – Two-way array factor patterns in both the azimuthal plane and elevation plane

In the presence of noise, however, these high sidelobes may lead to erroneous direction estimates. Fig. 21 shows the probability of such error for different values of signal-to-noise ratio, as calculated from a Monte Carlo simulation. Note that the probability of error in elevation is higher, due to the higher sidelobe level in the elevation scan. Although these errors are not desired, they are not detrimental to the system performance. Indeed, these erroneous direction estimates can simply be filtered out by the radar's tracking filter.

Clutter does not significantly affect the direction estimate. Indeed, if the target was detected, then the clutter in the sidelobe is much lower (10 dB or more) than the target signal. This has no appreciable effect on the direction-of-arrival estimation. Thus, with regard to clutter, we are concerned primarly about obscuration of the target (13.2.1).

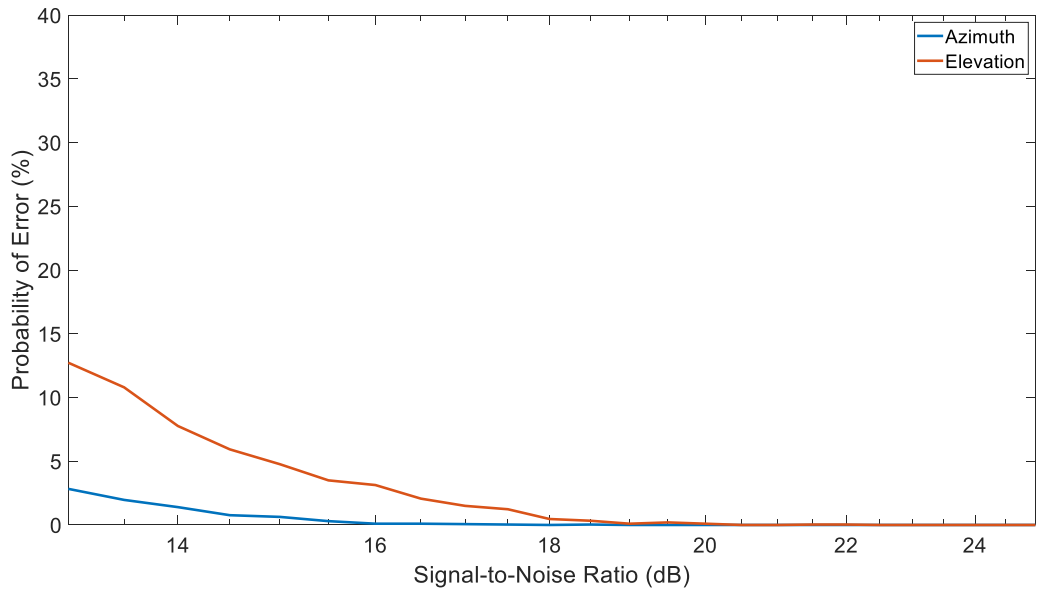

Fig. 21 – Probability of erroneous direction-of-arrival estimate due to system noise derived from Monte Carlo simulation.

13.3 Direction-of-Arrival Accuracy

The standard deviation of the direction-of-arrival estimation is presented in Fig. 22. Note that the accuracy is better in azimuth, since the 4 RX antennas are responsible for scanning in azimuth and form a longer baseline than the 3 TX antennas that are responsible for scanning in elevation.

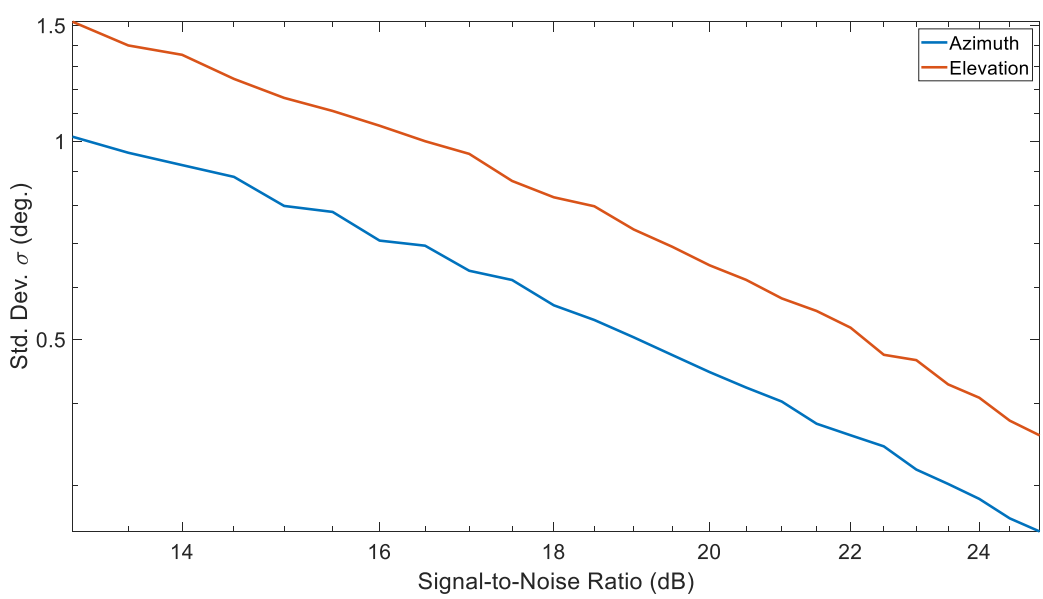

Fig. 22 – Standard deviation of direction-of-arrival estimation

13.4 Subarray Design

Proper design of the antenna subarrays is not trivial. The elements should be designed to maximize impedance bandwidth and tolerance to fabrication error. To this end, the input reflection coefficient S_{11} must wrap around the center of the Smith Chart.

To begin, let's equate the antenna subarrays to their equivalent circuit model, shown in Fig. 23 for the RX antenna subarray and Fig. 24 for the TX antenna subarray. In the circuit model, the patches are represented by low-impedance transmission lines, with 180° electrical length at resonance and radiation represented by shunt resistances. An inset feed is represented by a short-circuited series stub transmission line, yielding a series impedance of $jZ_4 \tan \beta_4 l_4$. We desire a subarray with radiation directed to broadside, so we must obey the following criteria:

- $\beta_1 l_1 = 360°$
- $\beta_2 l_2 = \beta_5 l_5 = 180°$

We also establish a second design criterion to promote tolerance to fabrication error: the return loss should be symmetric on either side of the design frequency. It can be shown that this occurs if and only if the combination of the transmission line 3 and the inset feed (represented by the series stub) can be modeled as transmission line of electrical length that is a multiple of a quarter-wavelength. To minimize the size of the subarray, we choose $\lambda/4$. The size of the inset feed is chosen to produce a broad bandwidth and low return loss.

The input reflection coefficient for both the RX and TX subarrays is shown on Smith Charts in Fig. 25 and Fig. 26 and on magnitude plots in Fig. 27 and Fig. 28. These plots show a 10 dB return loss bandwidth of approximately 4 GHz for each subarray.

Note that an antenna taper could also be applied by varying the width of the subarray patches. However, no taper is employed in this design.

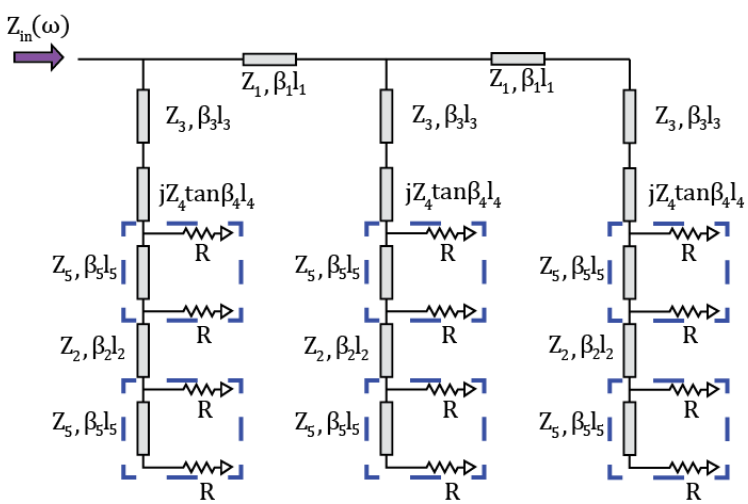

Fig. 23 - Equivalent circuit model for RX antennas

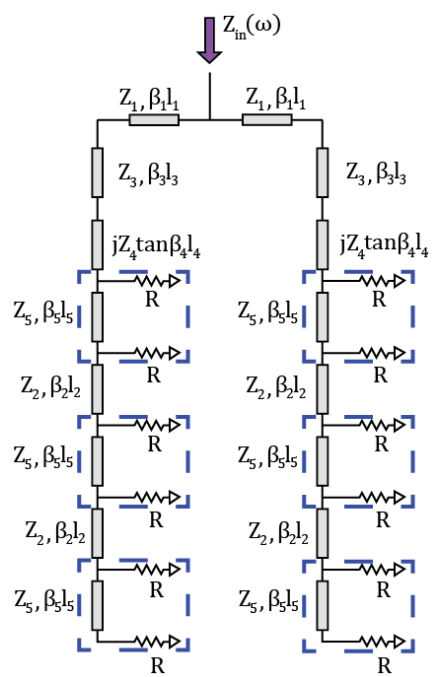

Fig. 24- Equivalent circuit model for TX antennas

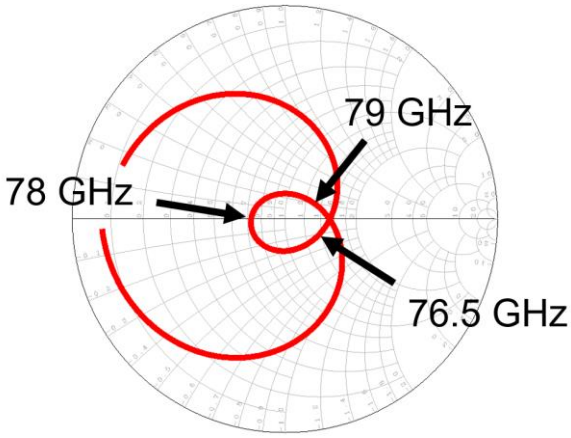

Fig. 25 – Input reflection coefficient (S_{11}) for the RX subarray

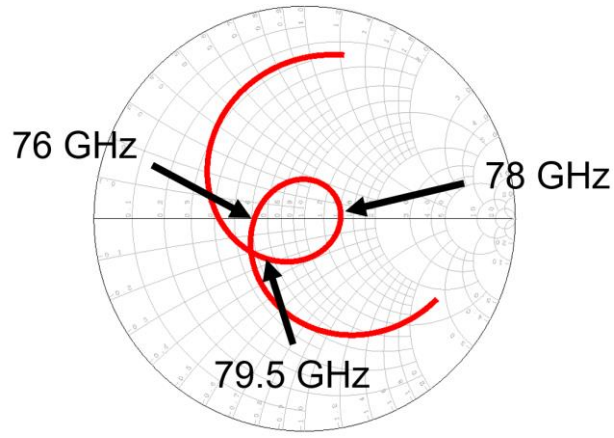

Fig. 26 - Input reflection coefficient (S_{11}) for the TX subarray

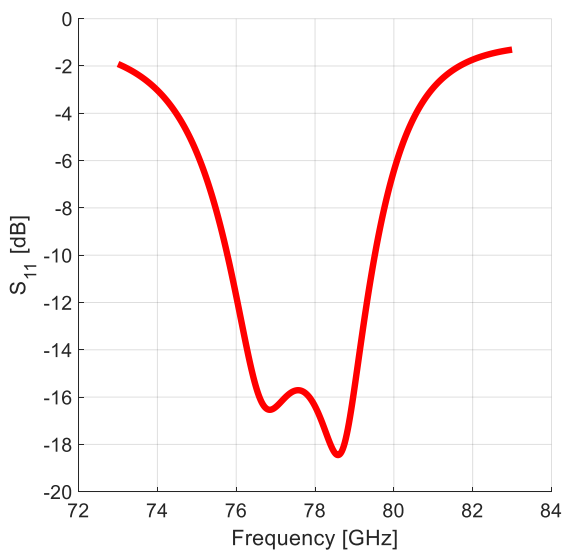

Fig. 27 - Input reflection coefficient (S_{11}) in dB for RX subarray

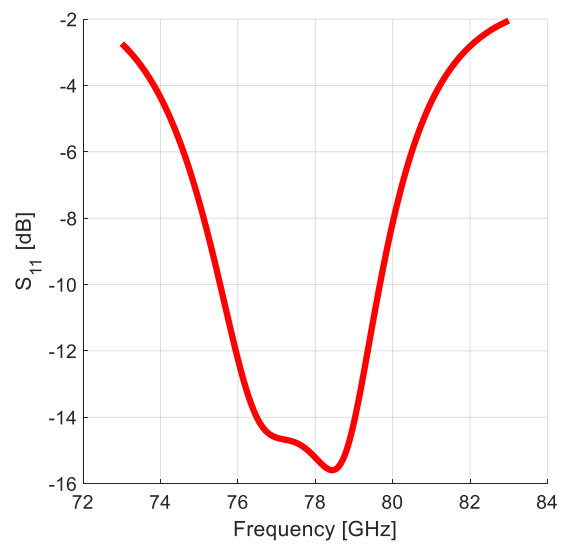

Fig. 28 - Input reflection coefficient (S_{11}) in dB for TX subarray

13.5 Extension to larger subarrays

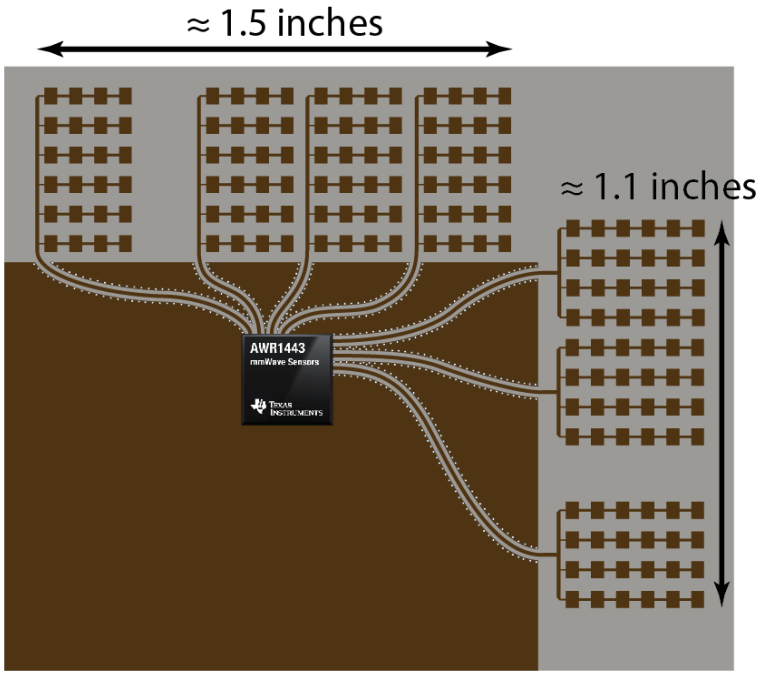

Fig. 29 - Artistic depiction of long-range radar (LRR) design

This design procedure can be extended to larger subarrays, such as those depicted in Fig. 29. This figure shows 4 by 6 subarrays for longer detection range but a subarray beamwidth of approximately 15° in azimuth and 15° in elevation.

14. TECHNOLOGY TRANSITION

The radar design presented in this report has been transitioned into a rapid reaction program sponsored by another DoD agency. The program objective is to utilize the mmW radar as an autonomy in collaboration with the Army Research Laboratory (ARL). Thus far, the program has demonstrated promising results, with the sensor capable of tracking a UAV target to a range of 45 meters. The radar prototype is shown in Fig. 30.

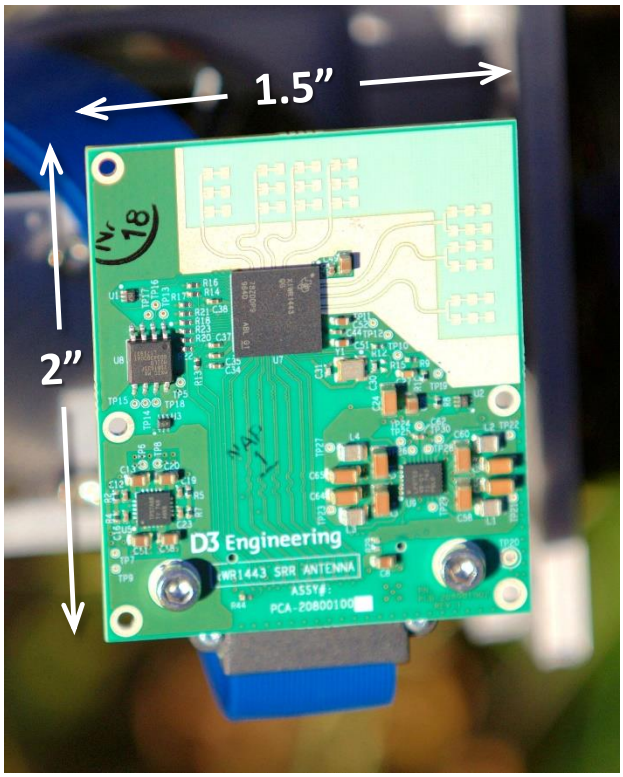

Fig. 30 - Radar prototype

15. IDEAS FOR IMPROVING DETECTION RANGE

Currently, the radar can track a small UAV drone that is within 45 meters range. However, potential transition partners will eventually desire a longer detection range, without sacrificing field of view. To this end, this section of the report identifies two separate design modifications that can be pursued to extend the radar detection range: (1) improving the antenna efficiency using air-filled substrate integrated waveguides and (2) extending the coherent integration time using a bank of second-order matched filters.

The ideas presented in this section have been proposed for NRL Base Program funding for FY20-22.

15.1 Air-Filled Substrate-Integrated Waveguide

The antennas and antenna feedlines are currently realized using microstrip technology. Although simple to fabricate and cheap, microstrip technology is lossy. For the Rogers RO4835 LoPro substrate employed in the radar design, Rogers estimates the loss to be 2.4 dB/inch at 78 GHz [8]. As a comparison, standard machined waveguides have a measured loss of 0.09 dB/inch at the same frequency [9]. We estimate that using microstrip instead of waveguide for the antennas and antenna feedlines results in 5 dB or more of system loss. Eliminating this loss would result in a detection range increase of 33%.

However, it is difficult to integrate machined waveguide with the radar PCB. A more feasible alternative is to use substrate-integrated waveguides (SIWs) [10]. SIWs are essentially waveguides manufactured using standard PCB processes. The top and bottom of the waveguide are made from the copper sheets of the PCB while the waveguide’s metallic side walls are emulated with rows of closely-spaced metallic vias. At W-band, the loss of SIWs has been measured to be close to 0.5 dB/inch [11]. This loss is almost entirely due to loss in the dielectric substrate, rather than conductive loss.

An even better alternative is to use air-filled substrate integrated waveguide (AFSIW) [12]. This recent technology is similar to standard SIW with the exception that the dielectric material inside the

waveguide has been largely replaced by air, thereby mitigating dielectric loss. Studies report measured losses as low as 0.13 dB/inch [12].

AFSIW technology presents several design challenges, such as: (i) manufacturability, (ii) mechanical stability, (iii) mitigation of grating lobes from slot subarrays, (iv) transition from the radar IC down into the AFSIW inner layer, and (v) efficient slot radiation. However, if these challenges can be overcome, the radar system could see an extension of radar range by as much as 30%-40%.

15.2 Extended Coherent Integration

Another way to extend the radar's detection range is to extend the coherent integration time. Indeed, each doubling of the coherent integration time yields 3 dB more radar system gain (19% more range). However, this is not simple, since phase coherence is difficult to maintain for long periods of time, especially at millimeter-wave frequencies.

Currently, the radar employs standard range-Doppler processing, which corrects for first-order (linear) chirp-to-chirp phase changes in the signal reflected from the target. As long as this first-order behavior is maintained, the system gain increases by 3 dB for every doubling of integration time. However, target and/or radar acceleration will inevitably occur. When this happens, gains of less than 3 dB (possibly negative) will occur for a doubling of the integration time.

However, if the radar system can correct for second-order chirp-to-chirp phase changes, then the limit on coherent integration time can be extended. This is evident in [13], in which the radar corrected for second-order phase changes resulting from the acceleration of an aircraft. However, this acceleration was known *a priori*. The distinction here, and the challenge, is that relative acceleration is not known *a priori*. Nevertheless, with sufficient computational resources, a large bank of matched filters can be used to correct for second-order phase deviation.

15.2.1 Received Signal Derivation

To derive this bank of matched filters, we must derive the form received radar signal under second-order motion. A series of transmitted FMCW chirps is proportional to

$$v_{TX}(t + mP) = \exp(2\pi f_1 t + \frac{\pi\beta t^2}{\tau}) \tag{7}$$

where m denotes the mth chirp and P is the chirp periodicity. The returned signal is time-delayed and proportional to

$$v_{RX}(t + mP) = \exp(2\pi f_1 (t - t_d) + \frac{\pi\beta (t - t_d)^2}{\tau}) \tag{8}$$

where t_d is the time delay between transmitting the signal and receiving a signal return. After stretch processing, the received signal is proportional to:

$$y(t) = \exp(2\pi f_1 t_d + \frac{\pi\beta}{\tau}(2t_d t - t_d^2)) \tag{9}$$

For a target at range R with range-rate v and range-acceleration-rate a, t_d is given by:

$$t_d = \frac{2(R + vt + {}^1\!/_2\, at^2)}{c} \tag{10}$$

Expression (10) can be generalized to the Mth order as

$$t_d = \frac{2}{c}\sum_{m=0}^{M}\frac{a_m}{m!}t^m \tag{11}$$

However, we will simply use (10) here, as we only wish to look at second-order phase correction.

15.2.2 Matched Filter Derivation

To derive the matched filter, we must discretize time as follows:

$$t[\vec{n}] = n_1T_1 + n_2T_2 + n_3T_3 \qquad (T_1 < T_2 < T_3) \tag{12}$$

Here, T_1 represents fast time sampling rate and T_2 represents slow time sampling rate in the traditional radar sense. T_3 represents the next step beyond this: a slower-time sampling rate that can be thought of as sampling acceleration.

Substituting (10) and (12) into the conjugate of (9) yields a matched filter for a target characterized by second-order motion.

$$Y[R,v,a] = \sum_{n_1=0}^{N_1-1} e^{-j4\pi(\frac{\beta}{c\tau}n_1T_1)R}\sum_{n_2=0}^{N_2-1}\sum_{n_3=0}^{N_3-1} y[\vec{n}]e^{-j4\pi(\frac{f_1}{c}+\frac{\beta}{c\tau}n_1T_1)\left(v(n_1T_1+n_2T_2+n_3T_3)+a/2(n_1T_1+n_2T_2+n_3T_3)^2\right)} \tag{13}$$

However, we must discretize the R, v, and a variables. The discretization is established as follows:

$$\frac{k_1}{N_1} = \frac{2\beta R}{c\tau}T_1 \tag{14}$$

$$\frac{k_2}{N_2} = \frac{2f_1vT_2}{c} \tag{15}$$

$$k_3 = \frac{2af_1T_2N_2T_3N_3}{c} \tag{16}$$

This discretization can be generalized for higher-order cases as follows:

$$k_m = \frac{2a_{m-1}f_1\prod_{i=1}^{m}T_iN_i}{c} \tag{17}$$

15.2.3 Experimental Results

The second-order matched filter was coded in MATLAB and tested using data recorded by Prototype 1 during the first year of this Karle Fellowship. The target is a small UAV situated 40 meters from the radar.

The results provided in Fig. 31 show that a greater than 6 dB SNR improvement using the second-order matched filter, which is referred to here as a range-Doppler-acceleration map technique.

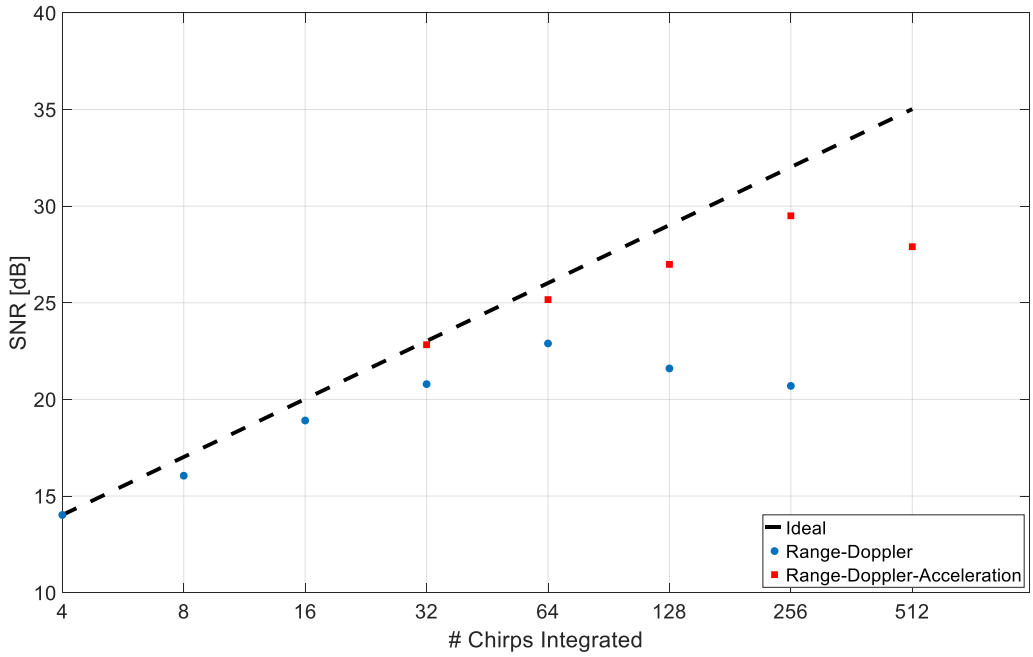

Fig. 31 - Experimental results for second-order matched filter show a more than 6 dB SNR increase compared to standard range-Doppler map techniques. The radar employed was Prototype 1 from the first year of the Karle Fellowship. The target is a small UAV situated 40 meters from the radar.

16. PUBLICATIONS

A conference paper discussing the results of Prototype 1 has been accepted to the conference Radio & Wireless Week 2019:

- **B. B. Tierney** and C. T. Rodenbeck, "3D MIMO Radar for UAV Obstacle Avoidance and Formation Flight" in *Radio & Wireless Week 2019*, Orlando, FL, January 20-23, 2019.

A patent has also been filed:

- **B. Tierney**, C.T. Rodenbeck, and D.F. Crouse, "MIMO radar array antenna for 3-dimensional sensing in autonomous airborne vehicles," US Non-Provisional Patent Application 62/599995, Navy Case Number 106334.

Many other results from this Karle Fellowship are intended to be published in the public literature, pending approval through the proper chain of command. In particular, journal publications will be pursued for the following topics:

- Antenna design procedure and design tradeoffs for MIMO radar with limited antenna channels
- Extended coherent integration using second-order phase correction
- Disambiguation of target range rate using radar tracking filter

17. SUMMARY AND CONCLUSIONS

The research sponsored by this Karle Fellowship has demonstrated the utility of automotive technology for accurate onboard sensing that enables UAV autonomy applications such as UAV tracking, formation flight, collision avoidance.

In the first year, a radar prototype (Prototype 1) was designed to maintain a broad field-of-view (FOV) in azimuth while sacrificing FOV in elevation to maintain a high antenna gain without the need for additional antennas. This reduces the cost of the sensor with minimal sacrifice to the performance for UAV applications such as swarming, sense-and-avoid, and tracking. Experimental results show FOV in its azimuthal plane of approximately 80° and the FOV in its elevation plane is approximately 20°. Angular estimation is achieved in both azimuth and elevation, but azimuthal estimation shows a smaller variance. The radar could detect a DJI Flame Wheel drone out to a distance of 50 meters.

In the second year, a radar prototype (Prototype 2) was designed using mmW ICs from Texas Instruments and a GPU from NVidia. The prototype is comprised of 4 RX antennas and 3 TX antennas. Experimental results show that a detection range of 45 for a small UAV target. However, due to the limited number of antenna channels, the field of view was limited to 30° by 30°.

Two research paths were presented for extending radar detection range without the addition of amplifiers or more antenna channels: (1) improving the antenna efficiency using air-filled substrate integrated waveguides and (2) extending the coherent integration time using second-order phase correction. Preliminary results are promising for extending the coherent integration time. These ideas have been proposed for funding from the NRL base program.

18. REFERENCES

[1] Inras, GmbH, [Online]. Available: www.inras.at/en/products/modular-radar-system.html.

[2] Inras, GmbH, "MIMO-77-TX4RX8 Frontend (User Manual)," [Online]. Available: http://www.inras.at/uploads/media/MIMO-77-TX4RX8_01.pdf.

[3] Rogers Corporation, "RO3003 Series Circuit Materials," [Online]. Available: https://www.rogerscorp.com/documents/722/acs/RO3000-Laminate-Data-Sheet-RO3003-RO3006- RO3010-RO3035.pdf.

[4] C. A. Balanis, Antenna Theory, Hoboken, New Jersey: John Wiley & Sons, 2005.

[5] U. Nickel, "Monopulse Estimation with Adaptive Arrays," *IEE Proceedings F - Radar and Signal Processing,* vol. 140, no. 5, pp. 303-308, 1993.

[6] M. A. Richards, Fundamentals of Radar Signal Processing, McGraw-Hill Education, 2014.

[7] J. G. Proakis and D. G. Manolakis, Digital Signal Processing, Upper Saddle River, New Jersey: Pearson Prentice Hall, 2007.

[8] Rogers, "Microwave Impedance Calculator," [Online]. Available: https://www.globalcommhost.com/rogers/acs/techsupporthub/en/mwi_calc2017.php.

[9] S. Verploegh, M. Coffey, E. Grossman, and Z. Popović, "Properties of 50-110-GHz Waveguide Components Fabricated by Metal Additive Manufacturing," *IEEE Transactions on Microwave Theory and Techniques,* vol. 65, no. 12, pp. 5144-5153, 2017.

[10] M. Bozzi, A. Georgiadis, and K. Wu, "Review of Substrate-Integrated Waveguide Circuits and Antennas," *IET Microwaves, Antennas & Propagation,* vol. 5, no. 8, pp. 909-920, 2011.

[11] Y. She, J. Hirokawa, and M. Ando, "Millimeter-wave transmission-loss evaluation of microstrip lines and post-wall waveguides and effects on efficiency of post-wall waveguide slot arrays," *Antennas and Propagation Society International Symposium,* 2009.

[12] F. Parment, A. Ghiotto, T. Vuong, and J. Duchamp, "Air-Filled Substrate Integrated Waveguide for Low-Loss and High Power-Handling Millimeter-Wave Substrate Integrated Circuits," *IEEE Transactions on Microwave Theory and Techniques,* vol. 63, no. 4, pp. 1228-1238, 2015.

[13] M. Malanowski, K. Kulpa, and K. E. Olsen, "Extending the Integration Time in DVB-T-based passive radar," *Europen Radar Conference (EuRAD),* 2011.

[14] Z. Chen et al., "A dual-polarized wideband substrate-integrated-waveguide-fed slot antenna array for 60 GHz," *2017 10th Global Symposium on Millimeter-Waves,* pp. 74-75, 2017.